HiSST: 2nd International Conference on
High-Speed Vehicle Science & Technology
11–15 September 2022, Bruges, Belgium

Experimental Boundary Layer Investigation of a Stacked Transpiration Cooling Setup with Uniform Blowing Ratio

Andreas Schwab [1], *Jonas Peichl* [2], *Markus Selzer* [2], *Hannah Böhrk* [2], *Jens von Wolfersdorf* [1]

Abstract

Transpiration cooling is considered as an innovative cooling method meeting the demand for efficient cooling of future rocket engine combustion chambers. In this context an experimental baseline study with a stacked transpiration cooled setup of four aligned ceramic fiber reinforced carbon (C/C) samples is investigated in hot gas conditions of $T_{HG} \approx 374.15\,\mathrm{K}$ and $\mathrm{Re}_{Dh} \approx 200.000$ with a transpiring coolant blowing ratio of $F = 0 - 4\%$ of air. Hereby, the focus is on the investigation of the boundary layer situation based on the measurement of velocity and temperature profiles with a measurement rake comprising a pitot tube and a thermocouple. A determination of the friction coefficient c_f as well as the Stanton number St is discussed and implemented for the no blowing and blowing cases. On the basis of two test cases with different transpiration lengths and starting points of uniform transpiration cooling a unifying illustration is aimed for the derived momentum and mass transfer parameters. Representations considering the momentum thickness Reynolds number Re_{δ_2} and the enthalpy thickness Reynolds number Re_{δ_h} yielded good agreement.

Keywords: *transpiration cooling, Ceramic composite material, turbulent boundary layers, friction coefficient, Stanton number*

Nomenclature

Latin

a – Thermal diffusivity
$a_0, a_1, B, B^{'}, C, C^{+}, C_{\Theta}^{+}$ – Constant
A – Cross sectional area
b_f, b_h – Modified blowing parameter
B_f, B_h – Blowing parameter
c_f – Friction coefficient
c_p – Isobaric heat capacity
D – Diameter
D_h – Hydraulic Diameter
F – Blowing ratio
H – Height
k – Thermal conductivity
K_D – Darcy coefficient
K_F – Forchheimer coefficient
L – Length
$\dot{m}$ – Mass flow rate
n – Power law index
p – Pressure
Pr – Prandtl number
r – Recovery factor
R – Specific gas constant
Re – Reynolds number
St – Stanton number
t – Thickness
T – Temperature
T_τ – Wall friction temperature
u – Velocity
u_{bulk} – Bulk velocity
u_τ – Wall friction velocity
v_w – Vertical injection velocity
W – Width
x, y – Rectangular coordinates

Greek

$\alpha, \beta, \chi, \psi$ – Constant
α – Dimensionless velocity gradient
δ – Boundary layer height
δ_2 – Momentum thickness
δ_h – Enthalpy thickness
ϵ – Deflection ratio
Θ – Dimensionless temperature
κ – Isentropic exponent
κ – Kármán constant of momentum transfer
κ_Θ – Kármán constant of heat transfer

[1] *Institute of Aerospace Thermodynamics, Pfaffenwaldring 31, 70569 Stuttgart*
[2] *DLR Institute of Structures and Design, Pfaffenwaldring 38, 70569 Stuttgart*

μ – Dynamic viscosity
ν – Kinematic viscosity
ρ – Density
τ – Wall shear stress
Superscripts
$+$ – Dimensionless wall coordinate
Subscripts
c – Center position
C – Coolant
HG – Hot gas
nw – Near wall position
r – Recovery
s – Static
t – Total
T_{01} – Referring to the thermal boundary layer
W – Wall
0 – No blowing reference case
$1-4$ – Order of sample arrangement
99 – Referring to the kinematic boundary layer
∞ – Fluid flow outside the boundary layer

1. Introduction

Whilst transpiration cooling was already investigated in the 1950s comparing different cooling methods Eckert and Livingood [1] stated the great potential of this cooling method. However, due to a lack of appropriate materials an application was quite rare. A revival of this cooling technique arose with the development of ceramic composite materials in the late 1990s as shown in Schweikert [2]. In this context the DLR Institute of Structures and Design (BT) manufacturing and measuring porous ceramic structures envisioned an application of transpiration cooling in the propulsion system of future transportation systems under extreme heat loads. In respective baseline investigations of Langener [3] and Schweikert [2] the general applicability and thermophysical characterization of flat porous ceramic reinforced carbon (C/C) samples for such applications was demonstrated under subsonic and supersonic flow conditions.
Continuing the road, at a more application related system investigations of a stacked transpiration cooling setup with interchangeable porous samples and individual controllable blowing ratios are performed. Therefore a detailed knowledge of the kinematic and thermal boundary layer situation is prerequisite and investigated with a measurement rake for velocity and temperature determination including vertical corrections according to McKeon et al. [4] and Bailey et al. [5]. In order to make further statements regarding the momentum and mass transfer in a transpired boundary layer the dimensionless friction coefficient c_f and the Stanton number St are the considered meaningful quantities. They are derived with the velocity and temperature profiles by the Clauser [6] method for the logarithmic overlap law of velocity and temperature without blowing, whilst in cases of blowing the extended overlap laws according to Stevenson [7] and Bradshaw [8] are applied. In this context, in the 1970s a research group in Stanford by Kays, Moffat, Simpson and Whitten [9, 10, 11, 12] investigated similar transpiration cooling conditions looking for the descriptive behavior of the dimensionless quantities in the transpired boundary layer. Here, a dependency of the friction coefficient $c_f = c_f\left(\mathrm{Re}_{\delta_2}\right)$ of the momentum thickness Reynolds number Re_{δ_2} and the Stanton number $\mathrm{St} = \mathrm{St}\left(\mathrm{Re}_{\delta_h}\right)$ of the enthalpy thickness Reynolds number Re_{δ_h} was found. On the basis of two exemplary test cases a validation of the statements is examined and tested for their applicability as unifying representation in context of momentum and heat transfer.

2. Experimental Setup

The experimental test rig used for the transpiration cooling experiments is a roughly $10\,\mathrm{m}$ long test facility called Medium Temperature Facility (MTF) at the Institute of Aerospace Thermodynamics (ITLR) in Stuttgart. This facility consists of a heated wind tunnel with an interchangeable measurement section for implementation of the stacked transpiration cooling setup. Equipped with various measurement techniques inside the measurement section, inside the stack of transpiration cooled C/C (Carbon/Carbon) samples as well as optical measurement techniques attached to the test rig, the thermophysical phenomena within the porous C/C samples and the mixing zone of transpired coolant and hot gas flow can be measured.

2.1. Experimental test rig and measurement section

The Medium Temperature Facility (MTF) is a suction mode driven wind tunnel with a maximum mass flow of $1.5\,\mathrm{kg/s}$. Ambient air is sucked into the facility, characterized by a laminar mass flow meter LFE50MC2-6 of TetraTec Instruments and warmed up by an electrical heater of the type Schniewindt CSN803A with an electrical power input of $44\,\mathrm{kW}$. Via deflector plates, copper meshes and rectifying

elements the heated air is thermally homogenized and accelerated by a nozzle into the final geometry of the test section with a rectangular cross-section size of $A_{HG} = H \times W = 90 \times 60\,\text{mm}^2$. In the test section a multi stacked transpiration cooling test bed of permeable carbon fiber reinforced carbon (C/C) samples is embedded in the bottom wall and exposed to the hot gas flow of the test facility. The transpiration cooled porous test structure stretches out to a final length of $290\,\text{mm}$ containing four actively cooled samples of $A_C = L \times W = 67 \times 52\,\text{mm}^2$ size and $t = 10\,\text{mm}$ thickness each divided by $7\,\text{mm}$ separation of galvanization and dividing plates. An insight into the measurement section onto the porous sample surface is provided in Fig. 2. The coolant supply per porous sample is realized by four individual thermal mass flow controllers by either Wagner/Bronkhorst, type F-203AV-M50-RDG-55-V, or Teledyne-Hastings, type HFC-303, with an air mass flow rate of $\dot{m}_C = 0\text{-}10.75\,\text{g/s}$. As a cooling fluid compressed air is used provided by a rotary screw compressor. Adjacent to the measuring section the flow speed is reduced by a diffusor and the temperature is cooled down by a water cooler in order to reduce thermal loads for the vacuum pump. An overall impression of the experimental test rig is given by Fig. 1. For more detailed technical characteristics it can be referred to [2].

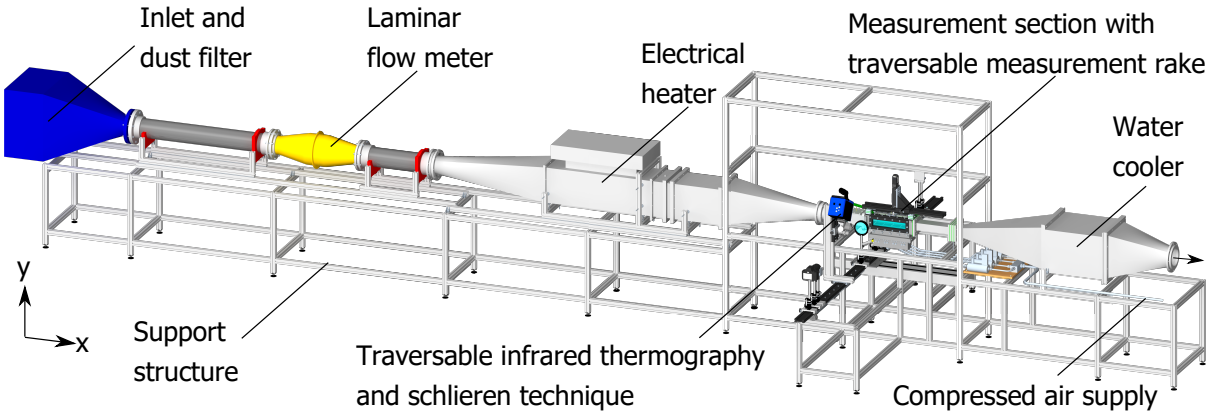

Figure 1. Dimetric view of the experimental test rig called Medium Temperature Facility (MTF)

2.2. Measurement equipment and instrumentation

In this work a focus is set on the boundary layer analysis in the interaction zone of hot gas flow and coolant. Therefore, three measurement techniques are applied: schlieren imaging, infrared thermography and measurements of temperature and velocity boundary layers with a measurement rake. Whilst schlieren imaging can visualize thermal boundary layers as demonstrated in [2], the infrared thermography evaluated by a differential method as proposed by Prokein et al. [13] visualizes the coolant efficiency of transpired coolant and is used as wall temperature reference for the considered investigations. However, focusing on the boundary layer situation of the transpired coolant, schlieren imaging measurements are left aside and only used as reference data.

Consequently, measured velocity and temperature profiles identified by a measurement rake as depicted in Fig. 2 are in the center of attention. It is consisting of a pitot tube with $0.5\,\text{mm}\,\pm 0.01$ outer diameter and $0.3\,\text{mm}\,-0\,+0.02$ inner diameter left-sided in flow direction for stagnation pressure measurements. A K-type thermocouple with $0.5\,\text{mm}$ outer diameter is mounted right-sided recording a recovery temperature T_r. Both measuring tubes are placed directly next to each other at the channel center line and approximately $20\,\text{mm}$ slightly bent forward into flow direction. Mounted in an axial guide carriage the measurement rake can be traversed in x-direction, manually, and in y-direction a precision linear actuator Owis LTM80 controls the vertical location by the Owis PS 10 controller with an accuracy of $1/128\,\text{mm}$. Herewith local kinematic and thermal boundary layers are measured in a near wall incremental step width of $\Delta y = 0.1\,\text{mm}$. The measurement rake additionally features an electrical wall detection system through an electrically closed circuit of the measurement rake tubes and the porous surface wall. In this regard an individual vertical zero point detection of each of the metallic tubes can be obtained.

2.3. Operation Conditions and Material

All measurements are conducted stationary with a corresponding warm-up time at an average pressure level of $81,128$ Pa due to the suction mode of the test facility. In this context the Reynolds number Re_{Dh} and the coolant blowing ratio F are the describing quantities. Both dimensionless values

$$\mathrm{Re}_{D_h} = \frac{\dot{m}_{HG}\, D_h}{A_{HG}\, \mu} \approx 200.000 \quad \text{and} \quad F = \frac{\text{transpired mass flux}}{\text{hot gas mass flux}} = \frac{\dot{m}_C / A_C}{\dot{m}_{HG} / A_{HG}} = 0 - 4\% \qquad (1)$$

involve the hot gas mass flow $\dot{m}_{HG}$ through its cross-sectional area A_{HG}. Whereas the Reynolds number Re_{Dh} definition extends the hot gas mass flux by a dynamic viscosity μ and a characteristic length of the hydraulic diameter D_h of the measurement cross-sectional area A_{HG}, the blowing ratio is defined as the ratio of transpired mass flux $\dot{m}_C / A_C$ and the hot gas mass flux. Both, coolant and hot gas mass flux, have a certain temperature level T_{HG} of the hot gas flow and T_C of the coolant flow. In this context, the dynamic viscosity μ of the hot gas is calculated by Sutherlands law with the according reference properties of air as given in [14, 15]. Considering the coolant mass flow the dimensionless blowing ratio ranges above a wide spectrum of $F = 0 - 4\%$. This corresponds to a coolant mass flow of up to $\dot{m}_C = 0 - 8.44$ g/s. Thereby, due to lateral heat conduction effects of the metallic surrounding the uncontrolled coolant temperature at the porous sample inlet surface ranges from $T_C \approx 293\,\mathrm{K} - 361\,\mathrm{K}$ depending on the coolant mass flow $\dot{m}_C$. In this measurement series two quite similar test cases are

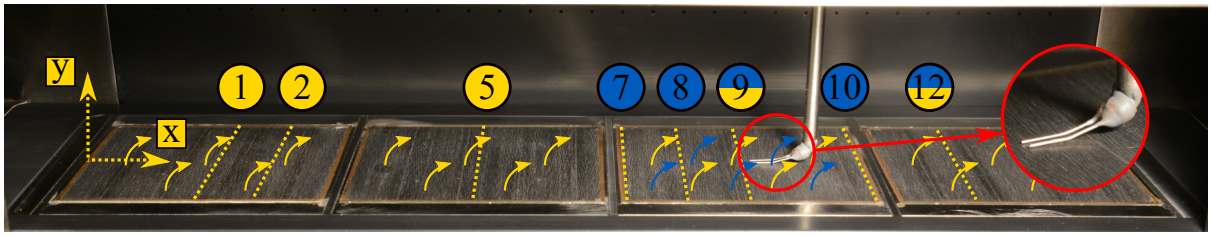

Figure 2. Measurement section of the Medium Temperature Facility (MTF) instrumented with a stacked transpiration cooling test bed as well as a temperature and velocity profile measurement rake; numbers and lines identify the axial measurement position of the two measurement sets in yellow and blue

considered and visualized in Fig. 2. While in the first case all four porous samples are transpiration cooled (Fig. 2: yellow), in the second case only the third sample is blown out (Fig. 2: blue). Because of a different blowing situation different measurement positions for the investigation of the velocity and temperature boundary layer by the measurement rake have been chosen. These positions are depicted in Fig. 2 and are chosen to be either at the beginning, after one quarter, in the middle or at the end of the relevant porous sample. For all cases reference measurements without blowing have been performed which is indicated by the blowing ratio of $F = 0\%$. An overview it the considered test conditions are presented in Tab. 1. In general, transpiration cooling can by applied by the use

No.	T_{HG} / K	Re_{D_h} / −	M / −	$\bar{u}$ / m/s	F / %	x / mm	Blowing
1	374.36	200,063	0.2060	79.83	0.00, 0.01, 0.15, 0.25, 0.50, 0.75, 1.00, 1.50, 2.00, 2.50, 3.00, 4.00	35, 50, 108, 182, 240	1., 2., 3., 4.
2	374.36	200,276	0.2081	80.65		148, 164, 182, 216, 240	3.

Table 1. Overview of both considered test configurations and its averaged test case parameters

of any porous material. However, in the context of an envisioned use in rocket combustion chambers permeable ceramic-matrix composite materials of carbon fiber reinforced carbon (C/C) are employed. These materials are manufactured and characterized by the DLR Institute of Structures and Design (BT) as described more detailed in [16, 17, 18]. The porous samples applied in this test case are characterized by its porosity of roughly $10.63\,\%$, its density of $1.383\,\mathrm{kg/m^3}$ and the permeability coefficients of Darcy and Forchheimer with $K_{D_y} = 5.153\mathrm{E}-13\ \mathrm{m}^{-1}$ and $K_{F_y} = 9.569\mathrm{E}-8\ \mathrm{m}^{-2}$ in average.

3. Analysis of Measurement-Data

In order to describe the boundary layer situation of transpired coolant into a hot gas flow the kinematic and thermal boundary layer needs to be investigated. Herewith a pitot tube and a K-type thermocouple as described in Sec. 2.2 measure a stagnation pressure $p_0(x,y)$ and a stagnation respectively recovery temperature $T_r(x,y)$ near the channel center line at different traversable x-positions along the y-expansion. Assuming an isentropic flow of an ideal gas in an one dimensional flow at a Mach number M the measured values can be transformed to either the static temperature

$$T_s(x,y) = T_r(x,y)\left[(1-r) + r\left(\frac{p_0(x,y)}{p_s(x)}\right)^{\frac{\kappa-1}{\kappa}}\right]^{-1} \tag{2}$$

or the local velocity boundary layer

$$u(x,y) = \sqrt{\frac{2\kappa}{\kappa-1} R T_s(x,y)\left[\left(\frac{p_0(x,y)}{p_s(x)}\right)^{\frac{\kappa-1}{\kappa}} - 1\right]}. \tag{3}$$

in dependence of the measuring values of static pressure $p_s(x)$, stagnation pressure $p_0(x,y)$ and recovery temperature $T_r(x,y)$. In this context the recovery factor r describes the percentage of energy transformation of kinetic energy into thermal energy reduced by the dissipative heat release in the boundary layer [19] and is quite commonly formulated by $r = \sqrt[3]{\mathrm{Pr}}$ in turbulent boundary layer flows [20, 21, 22]. Based on the operation conditions in Tab. 1 the thermophysical gas properties are provided by NIST REFPROP data base [23] assuming a constant Prandtl number $\mathrm{Pr} = 0.7$ as well as a specific gas constant of air with $R = 287,058\,\mathrm{J/(kg\,K)}$ and the isentropic exponent $\kappa = 1.397$. Moreover, on the assumption of a constant pressure gradient $\partial p / \partial y = 0$ based on to the boundary layer theory of Prandtl the local static pressure $p_s(x)$ stays constant within the boundary layer [24, 25] and is measured directly above the pitot tube protruding forward at the wall opposite the transpiration cooled samples.

3.1. Vertical height correction of the measurement rake

Whilst the measurement values itself remain uncorrected, the local vertical position has to be adapted from a control position towards their real y-position in the hot gas flow. In that regard three different vertical height corrections are applied considering a zero point detection, a geometric measurement level correction and an interference of the measurement tubes onto the flow phenomenology according to McKeon et al. [4] as well as Bailey et al. [5].

First of all a determination of the zero position, respectively the detachment point of both the thermocouple and the pitot tube from the wall has to be identified. Enabled by an electrical wall detection system an individual detachment point of the thermocouple and the pitot tube is detected and consequently the virtual control position is corrected by the individual zero point. In a second vertical height correction geometric limits concerning the discrepancy of the position controlled bottom edge of the measurement device versus the measurement level in the tube center as average value of the measuring cross section is resolved. As a result, the measuring point closest to the wall can only be half the pipe diameter $D_{tube} = 0.5\mathrm{mm}/2 = 0.25\mathrm{mm}$ as also stated in Meinert [26]. Finally, a third height correction according to McKeon et al. [4] and Bailey et al. [5] is applied. Here, two streamline deflections are considered, which are corrected by a derived deflection ratio $\epsilon = \Delta y / D$ of the vertical streamline shift Δy. On the one hand a deflection upwards arises due to a velocity shear with velocity gradients du/dy, which deflect higher velocity streamlines towards the measurement tube. In this context the deflection ratio ϵ is defined as

$$\epsilon = \frac{\Delta y}{D} = 0.15\tanh\left(4\sqrt{\alpha}\right) \quad \text{with} \quad \alpha = \frac{D}{2\,u(y_c)}\left.\frac{du}{dy}\right|_c, \tag{4}$$

using the local absolute velocity $u(y_c)$ referenced on the tube center c. Modified by Bailey et al. [5] Eq. 4 is valid for the range of $y / D_{tube} > 3$. On the other hand, focusing on the areas closer to the

wall with $y\,/\,D_{tube} \leq 3$ the velocity streamlines become deflected downwards by a near wall deflection ratio ϵ_{nw} due to blockage effects in the vicinity of the solid boundary. Consequently, in the near wall region both effects superimpose to the total near wall deflection

$$\epsilon_t = \epsilon - \epsilon_{nw} = 0.15 \tanh\left(4\sqrt{\alpha}\right) - \epsilon_{nw} \tag{5}$$

$$\text{with} \quad \epsilon_{nw} = 0.174\left(\frac{y}{D} - 3\right) - 1.25\left(\frac{y}{D} - 3\right)\left[0.15 \tanh\left(4\sqrt{\alpha}\right)\right] .$$

3.2. Representation of temperature and velocity profiles in the transpiration cooling setup

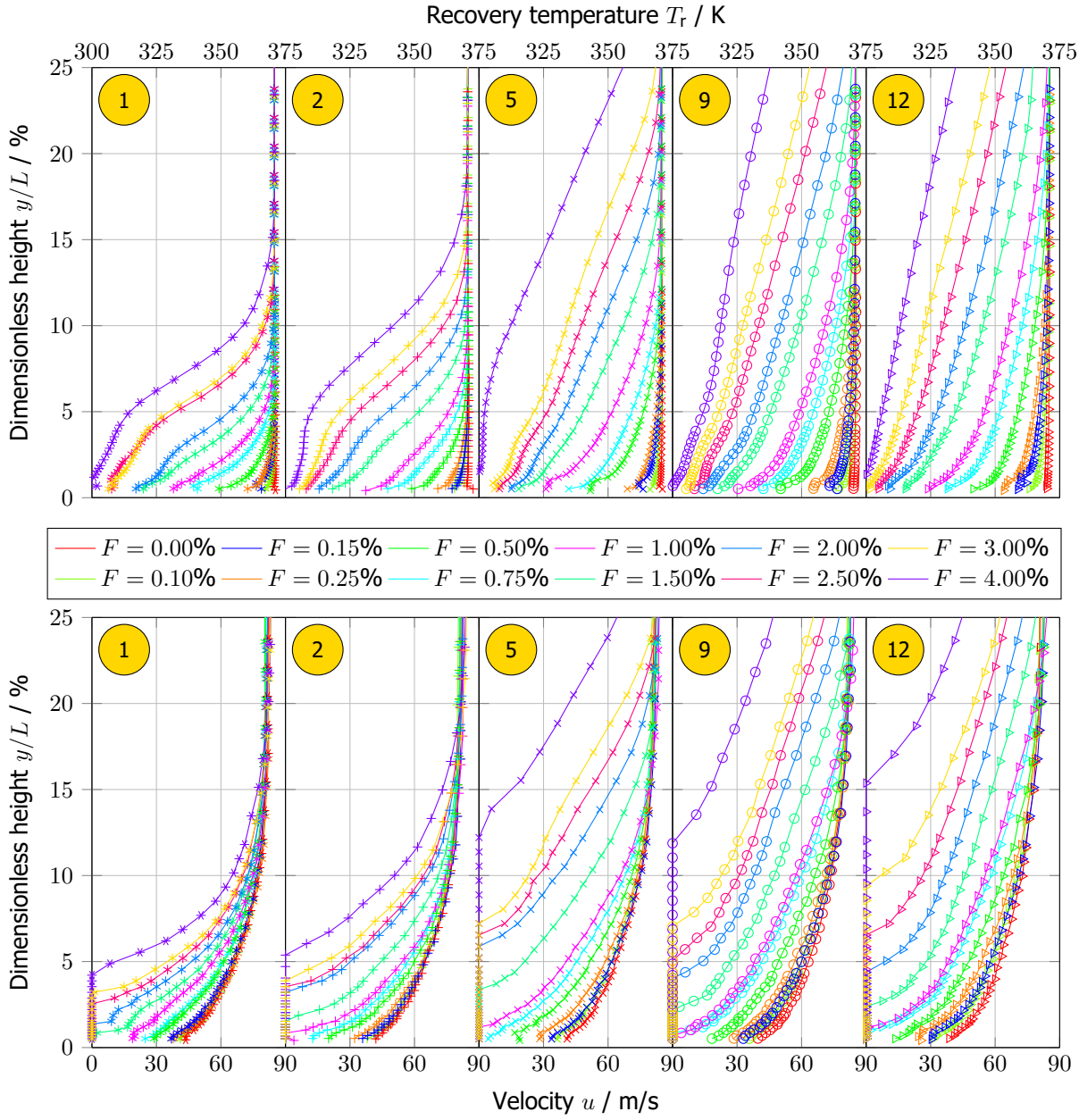

Figure 3. Experimental Overview of temperature and velocity boundary layers at the axial positions $x = 35\,\text{mm}, 50\,\text{mm}, 108\,\text{mm}, 182\,\text{mm}$ and $240\,\text{mm}$ according to test case 1 (see Fig. 2 and Tab. 1) for a variation of the blowing ratio F

To give a first impression of the temperature and velocity boundary layer situation in the stacked transpiration cooling setup test case 1 according to Tab. 1 is illustrated in Fig. 3 along the axial expansion as depicted in Fig. 2 by the yellow circles. Thereby, the recovery temperature $T_r(x,y)$ and the axial velocity $u(x,y)$ are shown in the lower channel quarter. Along the color bar of blowing ratios F the effects of transpiration cooling become obvious: with an increasing blowing ratio temperatures near the wall start to decrease and the local flow speed is reduced due to the orthogonal injection. The distinctive aspect of the measurements considered here is the stacked setup of multiple cooled samples with an accumulating film. Thus, the influence of the uniform blowing along the flow direction on the boundary layer growth in the velocity and temperature profiles, as well as the significantly cooler boundary layer and the gradually slower velocity close to the wall is evident. However, one looks at the shape of the temperature and velocity profiles an obviously different curve progression becomes recognizable. While the temperature profiles of lower blowing ratios exhibit a classical boundary layer progression, for higher blowing ratios an inflection point in the curve is visible. This is further supported by the velocity profiles of higher blowing ratios or moreover a progression in axial flow direction, where even negative flow velocities occur, respectively a higher static pressure $p_s(x)$ than a stagnation pressure $p_0(x,y)$ according to Eq. 3. In this representation the negative pressure gradients are depicted as zero velocity and not further considered in details. However, this clear indication of an adverse pressure gradient and boundary layer separation due to a reduced momentum of axial flow near the wall by the dominant vertical coolant transpiration is called blow off [9]. The turning point blowing ratio F in both the kinematic and thermal boundary layer illustration is between $F = 1,0 - 1,5$ %, which is supported by literature, e.g. Kays et al. [9], and can be confirmed in the following by the disappearance of the shear stresses at the wall (see Fig. 7). Nevertheless, due to the different flow patterns it has to be distinguished between the cases no blow off and blow off, whereby in this paper the focus is set in the no blow off boundary layers of smaller blowing ratios up to $F \leq 1$% whilst higher blowing ratios are neglected any further.

4. Boundary layer analysis

In order to characterize the depicted temperature and velocity profile in Fig. 3 a well founded boundary layer analysis is performed and visualized in Fig. 4. In this regard, a starting length calculation of the thermal and kinematic boundary layer growth is carried out, which emphasizes an unheated starting length situation of the test rig.

4.1. Identification of kinematic and thermal boundary layers

The velocity boundary layer criterion of Schlichting [27] as well as Gersten and Herwig [28] is adapted with the kinematic boundary layer height δ_{99} located at the point, where the local axial boundary layer velocity u reaches 99% of the external flow speed u_∞, respectively $u(y = \delta_{99}) = 0.99u_\infty$. Furthermore, the thermal boundary layer edge $\delta_{T_{01}}$ is defined in Gersten and Herwig [28] as point of local temperature deviation from the temperature on the outer edge T_∞ only by the amount of 1% to the maximum temperature difference of the wall temperature T_w to the external flow and given by $(T(x, y = \delta_{T_{01}}) - T_\infty) / (T_w - T_\infty) = 0.01$. However, in this context the transformation by Ghiaasiaan [29] with $(T(x, y = \delta_{T_{01}}) - T_w) / (T_\infty - T_w) = 0.99$ is more suitable. Visualizing the calculated boundary layer heights in Fig. 4 a steady increase of the boundary layer can be observed, which rather allows the comparison to a boundary layer growth of a flat plate than the consideration of a fully developed channel flow. Inferring from this a virtual boundary layer starting point can be derived. Based on an integration of the 1/7-power law the axial boundary layer growth is correlated with the proportionality of $\delta_{99} \approx \delta_{T_{01}} \sim x^{\frac{4}{5}}$ with the thermal and kinematic boundary layer heights being equivalent, since according to Kreith et al. [30] in turbulent boundary layer flows the turbulent fluctuations are the driving forces. Consequently applying the formulation by Schlichting [31]

$$\delta_{99} = 0.37\ \mathrm{Re}_{x_{99}}^{-\frac{1}{5}} x_{99} = 0.37 \left(\frac{x_{99} u_\infty}{\nu}\right)^{-\frac{1}{5}} x_{99} \sim x^{\frac{4}{5}} \tag{6}$$

a kinematic and thermal starting point of boundary layer can be determined. However, regarding the thermal boundary layer growth a different starting point $x_{T_{01}}$ in relation to the kinematic boundary layer is unmissable in Fig. 4. Concerning this matter Cebecci [32] correlated the ratio of the locally different

boundary layer heights

$$\frac{\delta_{T_{01}}}{\delta_{99}} = \left[1 - \left(\frac{x_{99} - x_{T_{01}}}{x_{99}}\right)^{4(n+2)/5(n+1)}\right]^{n/(2+n)} = \left[1 - \left(\frac{x_{99} - x_{T_{01}}}{x_{99}}\right)^{\frac{9}{10}}\right]^{\frac{7}{9}} \quad \text{with} \quad n = 7 \qquad (7)$$

to the axial difference of the starting points $x_{99} - x_{T_{01}}$. Consequently, both kinematic and thermal virtual boundary layer starting lengths can be calculated in dependency of the boundary layer heights δ_{99} and $\delta_{T_{01}}$. However, a concise calculation of the latter ones is rather vague and very error-prone due to measurement fluctuations and discontinuities. Therefor a determination of the kinematic starting length considering the entire velocity profile by integration of the momentum thickness is favored. Applying the power law with $n = 7$ again, Kays et al. [9] derived the connection of the axial Reynolds number $\mathrm{Re}_{x_{99}}$ and the momentum thickness as

$$\delta_2 = 0.036\ \mathrm{Re}_{x_{99}}^{-\frac{1}{5}} x_{99} = 0.036 \left(\frac{x_{99} u_\infty}{\nu}\right)^{-\frac{1}{5}} x_{99} \sim x^{\frac{4}{5}} \quad \text{with} \quad \delta_2 = \int_0^{\delta_{99}} \frac{\rho u}{\rho_\infty u_\infty}\left(1 - \frac{\rho u}{\rho_\infty u_\infty}\right) dy. \qquad (8)$$

This reduces any previous error dispersion and allows to determine the kinematic starting length by fitting Eq. 8 in a logarithmic representation of $ln(x_{99})$ versus $ln(\delta_2)$ to roughly $\Delta x_{99} = -410$mm. It has to be mentioned, that this is a virtual kinematic starting length featuring the local situation of the boundary layer consideration of the test channel for a test case without blowing and cannot be linked to an actual boundary layer starting length in the test rig. Subsequently applying Eq. 7 for the thermal boundary layer starting length a value of $\Delta T_{01} = -37.3$mm can be derived. Due to a thermal boundary layer that is much more difficult to determine, in particular due to thermal peculiarities of the test rig caused by tubular heating elements of the heater, a geometrical reference is utilized. Finally, instead of the calculated value the thermal starting point of thermal boundary layer growth is defined to $\Delta x_{T_{01}} = 85$mm in accordance with the end of the channel insulation shortly before the measurement section.

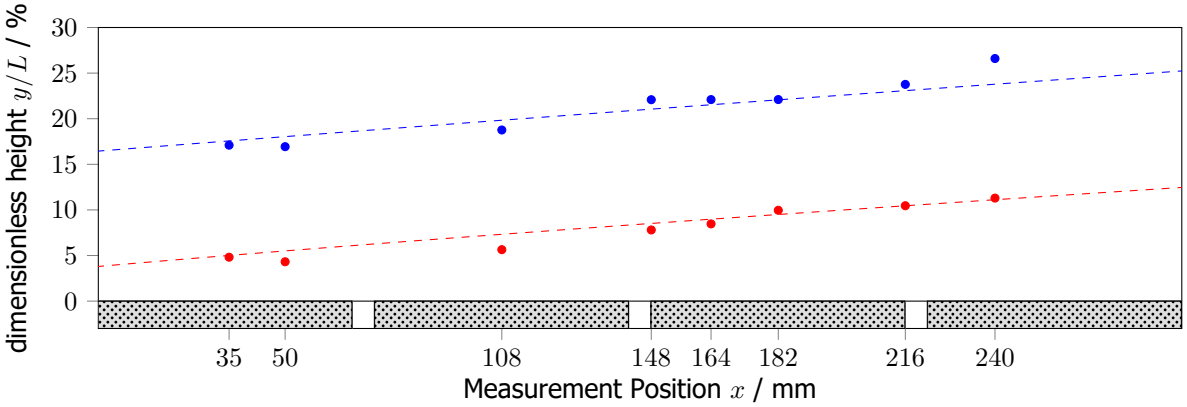

Figure 4. Identified kinematic (blue) and thermal (red) boundary layer height δ_{99} and $\delta_{T_{01}}$ at the marked axial measurement positions; dashed lines visualize the boundary layer growth with $x^{\frac{4}{5}}$ with its calculated starting length of $\Delta x_{99} = -410$mm and $\Delta x_{T_{01}} = -85$mm

All considerations and previous definitions are based on a power law, which is generally dependent on the Reynolds numbers and usually applied with $n = 7$ at $\mathrm{Re}_{D_h} \approx 50.000 - 110.000$ [31, 33]. However, according to Prandtl [33] also $n = 8$ or else can be used for higher Reynolds numbers Re_{D_h}. The assumption of a power law like $y^+ = C * (u^+)^{(1/n)}$ with $n = 7$ and a corresponding constant C is subject to multiple equations in this paper influencing both the constant prefactors and exponents. In this context, the exponent $n = 7$ proves good results, even though other values within the range of $n = 7 - 8$ might be applicable.

5. Dimensionless parameters in boundary layer flow: law of the wall for velocity and temperature

As interface of transpired coolant and hot gas flow the dimensionless wall conditions of the velocity boundary layer, the skin friction coefficient c_f, as well as for the thermal interface specification, the Stanton number St, are the determining parameters for the description of the local boundary layer situation. In this context Meinert [26] and Schweikert [2] considered similar conditions in their experimental test campaigns and contain a well researched overview of the identification of these parameters. In the following a brief overview is presented in characterizing both parameters by the methods of Clauser [6] and Stevenson [7] for the skin friction coefficient, as well as for the Stanton number by Clauser [6] and Bradshaw [8] respectively for the cases without and with transpiration cooling. Regarding temperature dependent material properties either the local static temperature $T_s(x,y)$ or the local wall temperatures measured by either the measurement rake or the infrared camera are used. Among others, this further concerns the local dynamic viscosity μ, the density $\rho(x,y)$ and the isobaric heat capacity $c_p(x,y)$, which is calculated by Sutherlands law [14], or is provided by NIST REFPROP [23] data base.

5.1. Skin friction coefficient calculation and representation

5.1.1. Skin friction determination for blowing ratio $F = 0\%$

In literature still often denoted as logarithmic law of the wall, Schlichting [27] renamed the intermediate layer for describing a turbulent boundary layer flow between the core flow and the near-wall viscous sublayer as the logarithmic overlap law. This provides a description of the dimensionless boundary layer coordinates

$$u^+ = \frac{1}{\kappa}\ln\left(y^+\right) + C^+ \quad \text{and} \quad y^+ = \frac{y u_\tau}{\nu} \quad \text{with} \quad u^+ = \frac{u}{u_\tau}, \quad u_\tau = \sqrt{\frac{\tau_w(x)}{\rho_w}} \quad \text{and} \quad c_f(x) = \frac{\tau_w(x)}{\frac{\rho_\infty}{2}u_\infty^2} \tag{9}$$

named by the wall friction velocity u_τ, the wall shear stress $\tau_w(x)$, the densities at the wall ρ_w and the boundary layer edge ρ_∞, the friction coefficient $c_f(x)$ as well as the free flow velocity u_∞. In this context the Kármán constant κ and the integration constant C^+ are set to $\kappa = 0.41$ and $C^+ = 5.0$ for smooth walls according to Schlichting [27]. Reformulating the expressions in Eq. 9 the dimensionless velocity

$$\frac{u(y)}{u_\infty} = \sqrt{\frac{c_f}{2}}\sqrt{\frac{\rho_\infty}{\rho_w}}\left[\frac{1}{\kappa}\ln\left(\mathrm{Re}_y\sqrt{\frac{c_f}{2}}\sqrt{\frac{\rho_\infty}{\rho_w}}\right) + C^+\right] \quad \text{with} \quad \mathrm{Re}_y = \frac{y u_\infty}{\nu} \tag{10}$$

is only a function of $u(y)/u_\infty = f\left(c_f/2\right)$. Consequently, with the velocity profile measurements $u(y)$ a best fit value of the friction coefficient $c_f(x)$ can be calculated.

5.1.2. Skin friction determination for blowing ratio $F > 0\%$

Based on the logarithmic overlap law in Eq. 9 according to Stevenson [7] the dimensionless boundary layer coordinate

$$u^+ = \frac{1}{v_w^+}\left\{\left[\frac{v_w^+}{2}\left(\frac{1}{\kappa}\ln\left(y^+\right) + C^+\right) + 1\right]^2 - 1\right\} \quad \text{with} \quad v_w^+ = \frac{v_w}{u_\tau}, \quad v_w = \frac{\dot{m}_C}{\rho_w A_c} \quad \text{and} \quad \rho_w = \frac{p_s}{R T_w} \tag{11}$$

can be extended by the dimensionless injection velocity v_w^+ at the injection surface. The injection velocity v_w of the coolant mass flux $\dot{m}_C$ is considered area-averaged by the outflow area A_C of the porous sample. Thereby local material properties as the local density at the wall surface ρ_w is taken into account and calculated by the local wall temperature T_w and its static pressure p_s at the wall. Rearranging the proposed equation for the dimensionless velocity

$$\frac{u(y)}{u_\infty} = \frac{c_f}{2}\frac{u_\infty}{v_w}\frac{\rho_\infty}{\rho_w}\left\{\left[\frac{1}{2\sqrt{\frac{c_f}{2}}}\frac{v_w}{u_\infty}\sqrt{\frac{\rho_w}{\rho_\infty}}\left(\frac{1}{\kappa}\ln\left(\mathrm{Re}_y\sqrt{\frac{c_f}{2}}\sqrt{\frac{\rho_\infty}{\rho_w}}\right) + C^+\right) + 1\right]^2 - 1\right\} \tag{12}$$

the friction coefficient c_f under the conditions of blowing can be identified by the measured velocity profiles.

5.1.3. Results of skin friction determination

Applying the overlap laws of Clauser [6] and Stevenson [7] by Eq. (10) and (12), exemplary the determination of the skin friction coefficient $c_f(x)$ is demonstrated in Fig. 5 for test case 2 (see Tab. 1 at the axial position of $x = 216$mm. By fitting the skin friction coefficient c_f for each measured velocity profile, data points closer to the wall can be targeted. In other words, the determination of the skin friction coefficient is massively dependent on the fitting range and fluctuations of the measurement points and by no means an unambiguous calculation of the friction coefficient value. However, for the measured velocity profiles (symbols) the representation of the dimensionless velocity $u(y)/u_\infty$ over the Reynoldsnumber Re_y referring to the local height y (left) shows good agreement with the logarithmic overlap laws by Clauser [6] and Stevenson [7] (lines) closer to the wall, until the transition to the core flow with an dimensionless velocity $u(y)/u_\infty = 1$ is reached. Presented for a variety of blowing ratios the effect of friction reduction for increasing blowing ratios is obvious in Fig. 5 reducing the near wall velocities significantly. Due to the strong decline of the wall friction and consequently the friction velocity u_τ, the dimensionless wall coordinate u^+ rises in reciprocal manner, which is shown in Fig. 5. As a result the dimensionless wall coordinates are only depicted until the blowing ratio of $F = 0.5$% for better visibility.

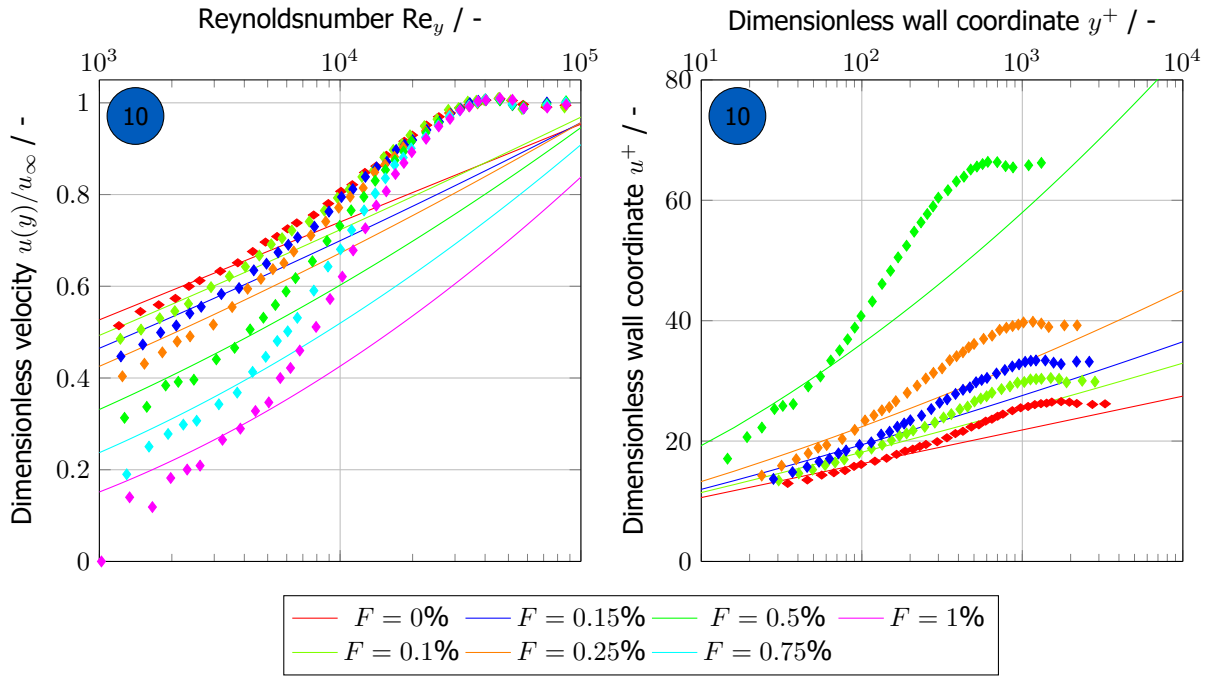

Figure 5. Clauser diagramms of the dimensionless velocity u/u_∞ (left) and the logarithmic overlap law (right) for different blowing ratios F at the axial position of $x = 216$mm at test case 2; lines mark the models in Sec. 5.1.1 and Sec. 5.1.2 according to Clauser [6] and Stevenson [7], whereas dots indicate the measurement data

5.2. Stanton number calculation and representation

5.2.1. Stanton number determination for blowing ratio $F = 0$%

Similar to the logarithmic overlap law for the kinematic boundary layer a match of the wall layer and the core layer for the thermal boundary layer can be obtained by a thermal overlap law for smooth walls according to Schlichting [19]. In this regard the dimensionless wall coordinates

$$T^+ = \frac{1}{\kappa_\Theta}\ln\left(y^+\right) + C_\Theta^+ \quad \text{with} \quad C_\Theta^+ = 13.7\,\mathrm{Pr}^{2/3} - 7.5 \quad \text{and} \quad y^+ = \frac{y u_\tau}{\nu}$$
$$\text{with} \quad T^+ = \frac{T - T_w}{T_\tau}, \quad T_\tau = \frac{\dot{q}_w(x)}{\rho_w c_{p_w} u_\tau(x)} \quad \text{and} \quad \mathrm{St}(x) = \frac{\dot{q}_w(x)}{\rho_\infty c_{p_\infty} u_\infty \left(T_\infty - T_w\right)} \tag{13}$$

are defined by the friction temperature T_τ as ratio of the wall heat flux $\dot{q}_w(x)$ and the wall friction heat flux $\rho_w c_{p_w} u_\tau(x)$. In this context the constant κ_Θ is representing the Kármán constant of heat flux established as $\kappa_\Theta = \kappa/\mathrm{Pr}_t = 0.47$ in Schlichting [27] and Gersten and Herwig [28]. Whilst the wall heat flux $\dot{q}_w(x)$ can be derived by the local Stanton number stated in Rohsenow et al. [34] accounting for the temperature difference at the free flow and the wall $T_\infty - T_w$, the dimensionless temperature

$$\Theta = \frac{T - T_w}{T_\infty - T_w} = \mathrm{St}\,\frac{c_{p_\infty}}{c_{p_w}}\sqrt{\frac{2}{c_f}}\sqrt{\frac{\rho_\infty}{\rho_w}}\left[\frac{1}{\kappa_\Theta}\ln\left(\mathrm{Re}_y\sqrt{\frac{c_f}{2}}\sqrt{\frac{\rho_\infty}{\rho_w}}\right) + 13.7\,\mathrm{Pr}^{2/3} - 7.5\right] \tag{14}$$

can be derived solely in dependence of the Stanton number St and the kinematic wall friction coefficient c_f by $\Theta(y) = f\,(\mathrm{St}, c_f)$. Any temperature dependent material properties at the free flow are further calculated either by the ideal gas law or gained by the thermophysical gas properties data base provided by NIST REFPROP [23] based on the locally measured temperature profile by the measurement rake or the wall temperatures by the infrared camera.

5.2.2. Stanton number determination for blowing ratio $F > 0\%$

Based on the measurement data and derived expression of Isaacson and Alsaji [35] for a dimensionless temperature in the inner layer of a transpired boundary layer, Bradshaw [8] reconsidered the mixing length model regarding the behavior of the heat flux and shear stress in the viscous sublayer and redefined the dimensionless temperature

$$T^+ = \frac{1}{v_w^+}\left[\left(1 + u^+ v_w^+\right)^{\mathrm{Pr}_t}(1+f) - 1\right] \quad \text{with} \quad f = v_w^+\,(B - B') + {v_w^+}^2 \quad \text{and} \quad B - B' = -1.1 \tag{15}$$

with the turbulent Prandtl number Pr_t in the exponent. Bradshaw [8] further defined the turbulent Prandtl number as ratio of $\mathrm{Pr}_t = \kappa/\kappa_\Theta$, which can be derived by both logarithmic overlap laws of Eq. (9) and (13) according to Schlichting [27] defining the turbulent Prandtl number as ratio of turbulent viscosity and turbulent thermal diffusivity. Consequently, the turbulent Prandtl number yields $\mathrm{Pr}_t = \kappa/\kappa_\Theta = 0.87$. In this context, the difference of both constants $B - B'$ is estimated by Bradshaw [8] for air with $\mathrm{Pr} \approx 0.7$ matching the considered test conditions here quite well. Subsequent, reformulating this stated overlap law for coolant injection the dimensionless temperature

$$\Theta = \mathrm{St}\,\frac{u_\infty}{v_w}\frac{c_{p_\infty}}{c_{p_w}}\frac{\rho_\infty}{\rho_w}\left[\left(1 + \frac{2}{c_f}\frac{u(y)\,v_w}{u_\infty^2}\frac{\rho_w}{\rho_\infty}\right)^{\mathrm{Pr}_t}\left(1 - 1.1\sqrt{\frac{2}{c_f}}\frac{v_w}{u_\infty}\sqrt{\frac{\rho_w}{\rho_\infty}} + \frac{2}{c_f}\frac{v_w^2}{u_\infty^2}\frac{\rho_w}{\rho_\infty}\right) - 1\right] \tag{16}$$

is derived in dependence of the local Stanton number and friction coefficient $\Theta(y) = f\,(\mathrm{St}, c_f)$, again, showing the close dependency of kinematic and thermal boundary layer behavior.

5.2.3. Results of Stanton number determination

Similar to Sec. 5.1.3 the local Stanton numbers St of test case 2 at the axial position of $x = 216$mm are presented in Fig. 6 for a wide variety of blowing ratios F. Therein a visualization of the dimensionless temperature Θ along the y-direction Reynolds number Re_y (left) as well as a representation of the dimensionless wall coordinates T^+ and y^+ (right) are depicted based on the calculated Stanton numbers St according to Clauser [6] and Bradshaw [8] in Eq. (14) and (16). In this case also a near wall optimization is implemented looking for an optimum fit of measured values closer to the wall and resulting in a fair well agreement in Fig. 6 left with continuously decreasing Stanton numbers for higher blowing ratios, respectively a decreasing dimensionless temperature Θ. Whilst already for a short blowout section of higher blowing ratios like $F = 1\%$ both the friction coefficient in Fig. 5 and the Stanton number tend to zero at Pos. 10 at $x = 216$ mm a first indication on a limit of coolant mass injection is discernible. This underlines the conclusions of Fig. 3 and confirms the limitation to blowing ratios of $F \leq 1\%$.

However, in general, a calculation and fit is extremely sensitive and anything but unambiguous with regard to the fitted values and the fitting range. Especially, temperature measurement with a determination of Stanton numbers is by far more difficult than a friction number calculation. This is even

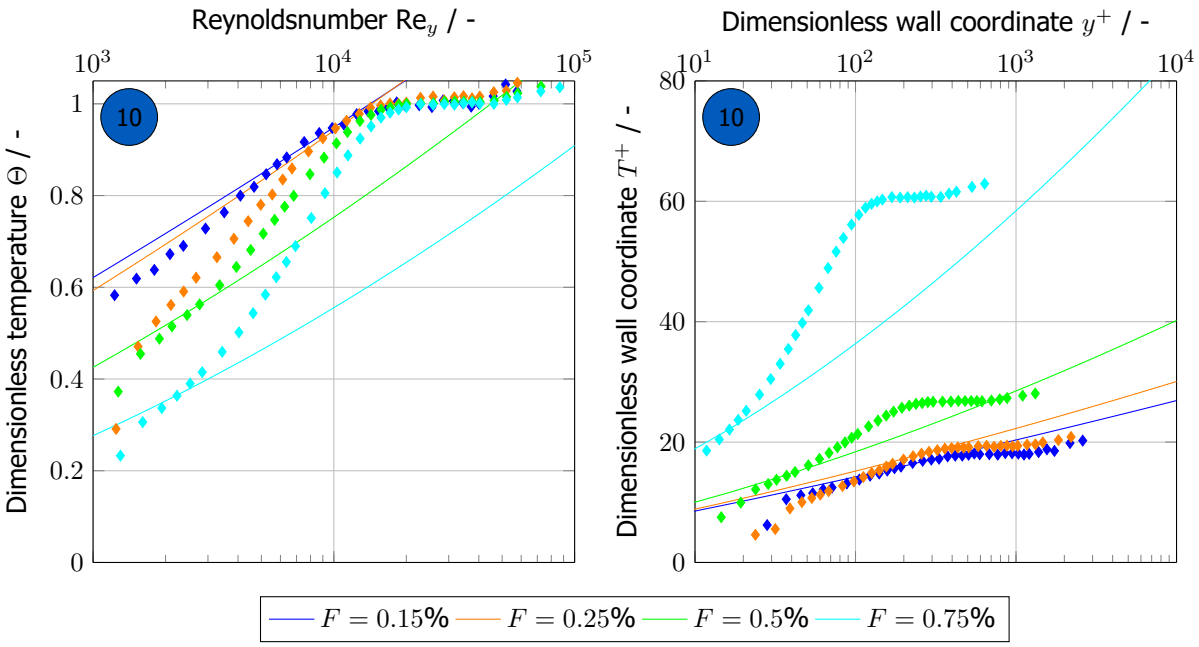

Figure 6. Clauser diagramms of the dimensionless temperature Θ (left) and the logarithmic overlap law (right) for different blowing ratios F at the axial position of $x = 216$mm at test case 2; lines mark the model in Sec. 5.2.2 according Bradshaw [8], whereas dots indicate the measurement data

more crucial for the cases without blowing. Causes for this can be found in rather small temperature gradients due to the low thermal conductivity at the wall and the moderate Mach number of the flow situation. A boundary layer identification is superimposed of higher measurement uncertainties relative to the temperature gradient and consequently the identification tends to be carried out more on a fluctuating straight line than a unequivocal profile. Consequently, Stanton numbers for the reference test case of $F = 0\%$ are not displayed in the following.

6. Friction coefficients in dependence of the axial Reynolds number $\mathrm{Re}_{x_{99}}$

One result of the considered measurements is the influence if transpiration cooling over a long transpiration distance. In this context the wall friction is decreasing with either increasing axial running length x or increasing blowing ratio F. Assuming the 1/7 power law, Kays [9] derived from the momentum integral equation in terms of the boundary layer thickness parameters the expressions

$$\frac{c_{f_0}}{2}\left(\mathrm{Re}_{x_{99}}\right) = 0.0287\ \mathrm{Re}_{x_{99}}^{-1/5} \qquad \text{and} \tag{17a}$$

$$\frac{c_f}{2}\left(\mathrm{Re}_{x_{99}}\right) = 0.0287\ \mathrm{Re}_{x_{99}}^{-1/5}\frac{\ln\left(1+B_f\right)}{B_f} \quad \text{with} \quad B_f = \frac{F}{c_f/2} \tag{17b}$$

for the axial skin friction development for the cases of no blowing and blowing. For the series of measurements considered here the behavior of the wall friction along the running length in form of the axial Reynolds number $\mathrm{Re}_{x_{99}}$ is depicted in Fig. 7 (left) and is compared to the correlations in Eq. (17a) and Eq. (17b). Herein, both mentioned test cases of Tab. 1 are depicted, indicating test case 2 with a transpiration start at a progressed axial running length with filled symbols. Whilst in similar experiments Simpson [10] confirmed the applicability of the correlations derived by the integral momentum theorem, here the measurement results also show a general match in terms of the measurement accuracy. However, two constraints have to be made. First of all the agreement is limited to small blowing ratios of $F = 0.5\%$. Although at the first measurement point still the measurement values meet theory, for higher blowing ratios the deviations of measurement and correlation increase especially with progressing running lengths. This divergence is further underlined by the second test case. Secondly, a difference of the first and second test case is obvious, especially recognizable at the joint measurement position of $x = 182$mm. As expected, the friction coefficients for test case 1 with longer axial running length and

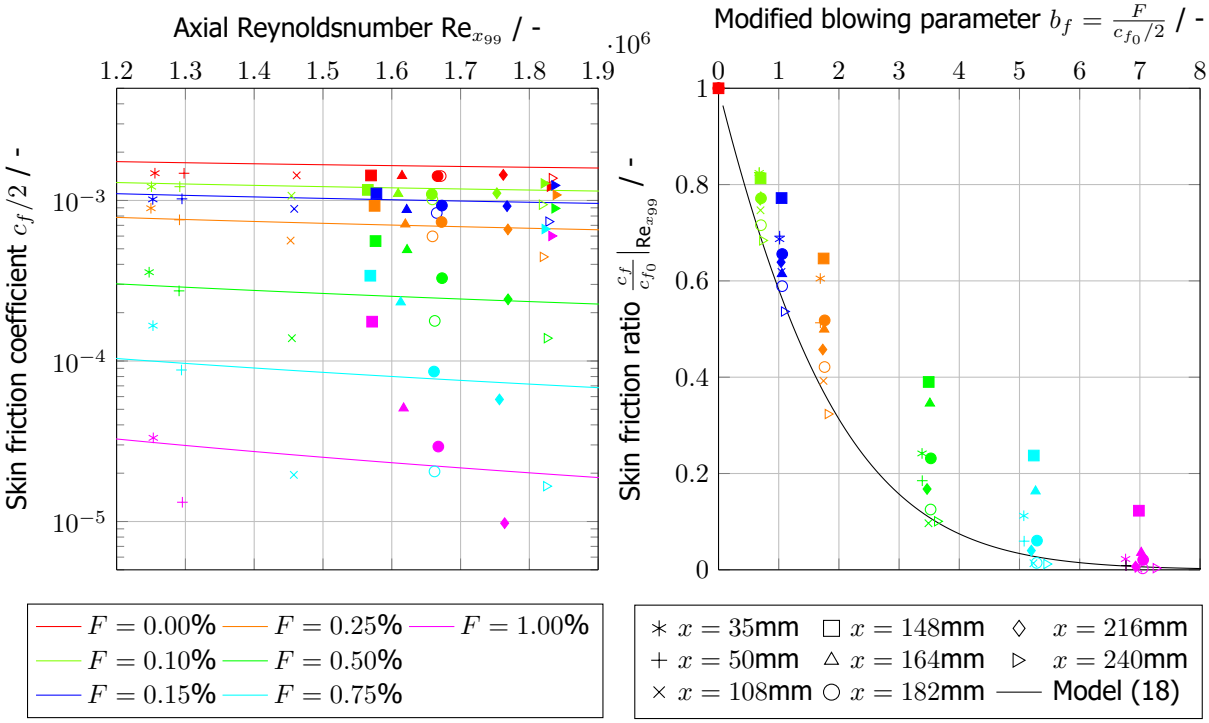

Figure 7. Representation of the skin friction development along the axial running length in comparison with the respective correlations in Eq. (17a) and Eq. (17b)(left) and the exponential friction reduction due to blowing at a specific location Re$_{x_{99}}$ (right); filled symbols indicate test case 2 (see Tab. 1))

an accumulated coolant film are smaller. However, this application is not captured by the correlations in Eq. (17a) and Eq. (17b), consequently questions regarding the comparability of both test sets over the axial run length can be raised.

To the illustration of the friction reduction due to blowing, both test cases are depicted in Fig. (7) (right) and are analyzed with the model in Eq. (18). This correlation is derived from a Couette flow assuming a constant density fluid and constant blowing along the running length [9]. The friction ratio of a transpiration cooled wall versus an uncooled wall at an identical axial position

$$\left.\frac{(c_f/2)}{(c_f/2)_0}\right|_{\mathrm{Re}_{x_{99}}} = \frac{b_f}{e^{b_f}-1} \quad \text{with the blowing parameter} \quad b_f = \frac{F}{(c_f/2)_0} \tag{18}$$

is describing the exponential friction reduction due to the transpired coolant with the blowing ratio F and also results from the division of both equations Eq. (17a) and Eq. (17b) and minor rearrangements. In this case the measurement values of c_{f_0} are used as reference values for the modified blowing parameter b_f. For both cases an exponential decay of the friction ratio can be confirmed. However, start-up effects of transpiration cooling building up cannot be missed especially for test case 2 and both early measurement points at $x = 35$mm and $x = 50$mm for test case 1. Consequently, the idea of overlapping two theoretically identical test cases with only one start up length shift cannot be realized by the upper models.

7. Friction coefficients in dependence of the momentum thickness Reynolds number Re$_{\delta_2}$

Aiming for a unifying illustration of both test cases the consideration of the incoming flow condition by the momentum thickness δ_2 of the velocity profile is key. In this context the overall shape and development of the flow profile is taken into account. As derived by Kays [9] in similar procedure as the previous determinations in Sec. 6, the assumption of a 1/7 power law and the use of the momentum

integral in terms of the boundary layer thickness parameters led to

$$\frac{c_{f_0}}{2}\left(\mathrm{Re}_{\delta_2}\right) = 0.0125\ \mathrm{Re}_{\delta_2}^{-1/4} \qquad \text{and} \tag{19a}$$

$$\frac{c_f}{2}\left(\mathrm{Re}_{\delta_2}\right) = 0.0125\ \mathrm{Re}_{\delta_2}^{-1/4}\left[\frac{\ln\left(1+B_f\right)}{B_f}\right]^{5/4}\left(1+B_f\right)^{1/4} \quad \text{with} \quad B_f = \frac{F}{c_f/2} \tag{19b}$$

for a situation without blowing and with blowing. In this context the momentum thickness Reynoldsnumber Re_{δ_2} is calculated by the momentum thickness δ_2 according to the definition in Eq.(8). The applicability of both correlations is proven in a multitude of publications by Simpson [10, 36, 37] even considering variable injection and suction. However, in order to achieve a better fit to own measurements, the prefactor is adapted from $C = 0.0125$ to $C = 0.0106$ by fitting the measurement data of the now blowing test data, even though a connection of the original prefactor and the 1/7 power law can be drawn. With the adapted prefactor the measurement results are opposed to both correlations in Fig. 8 and show great agreement. In addition to the previous observations in Sec. 6, the experimental data of the second test case are now also in good agreement with the theory. Exceptions only have to be made for higher blowing ratios of $F > 0.5\%$, which again show increasing deviations from the theoretical approach. An interesting side node has to be made on the measurement value for $x = 240\mathrm{mm}$ of the second test case above the fourth porous sample, which is not transpiration cooled any more. Here, the measurement values are falling back onto the values of the no blowing reference case quite rapidly for small blowing rates and slightly slower for larger blowing rates due to a more stable remaining cooling film.
Further, the friction reduction can be depicted as ratio of a transpiration cooled test case and the no

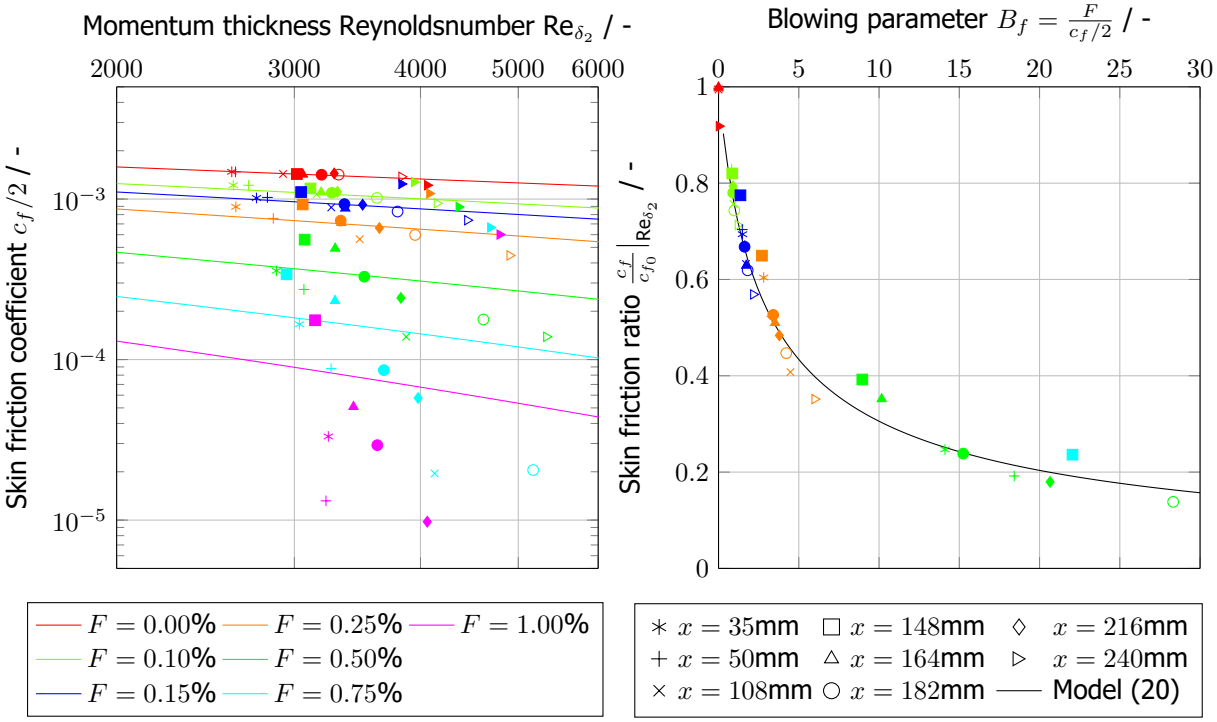

Figure 8. Illustration of the friction coefficient in dependence of the momentum thickness Reynoldsnumber Re_{δ_2} with adapted correlations in Eq. (19a) and (19b) by a prefactor $C = 0.0106$ (left) and the exponential friction reduction due to blowing at comparable momentum thickness Reynoldsnumber Re_{δ_2} (right); filled symbols indicate test case 2 (see Tab. 1)

blowing test case

$$\left.\frac{(c_f/2)}{(c_f/2)_0}\right|_{\mathrm{Re}_{\delta_2}} = \left[\frac{(1+B_f)}{B_f}\right]^{5/4}(1+B_f)^{1/4} \quad \text{with} \quad B_f = \frac{F}{c_f/2}. \tag{20}$$

Here, as reference value c_{f_0} the adapted correlation is used. Thereby, the reference value c_{f_0} has to be calculated for an identical momentum thickness Reynoldsnumber Re_{δ_2}, which is not related to the same axial position of the test case with and without blowing, but an imaginary axial position with $\mathrm{Re}_{\delta_2}(c_f) = \mathrm{Re}_{\delta_2}(c_{f_0})$. In comparison to Fig. 7 (right) the measurement values of both test cases coincide in Fig. 8 (right). Even though a slight transpiration cooling start-up effect is still visible, the advantages of a representation with the momentum thickness Reynolds number Re_{δ_2} are obvious and prove to be the preferred approach.

8. Stanton numbers in dependence of the axial Reynolds number $\mathrm{Re}_{x_{99}}$

Focusing on the momentum transfer effects of transpiration cooling in Sec. 6 and 7 the heat transfer is considered in the following for both presented test cases in Tab. 1. Again, a discussion on the heat transfer over the running length will be made first. Thereby in a range of publications Moffat, Kays and Whitten [12, 11, 38, 39] attempted to correlate the heat transfer to a transpired turbulent boundary layer. More closely described in [9] a derivation by the energy equation for turbulent flow and a Couette flow approximation with constant surface temperature leds to similar expressions as for the momentum transfer in Eq. (17a) and (17b) supplemented by the Prandtl number Pr. Additionally, due to the situation of an unheated starting length of the test section as described in Sec. 4 a correction term is added, yielding

$$\mathrm{St}_0(\mathrm{Re}_{x_{99}}) = 0.0287\,\mathrm{Re}_{x_{99}}^{-1/5}\mathrm{Pr}^{-2/5}\left[1-\left(\frac{x_{99}-x_{T_{01}}}{x_{99}}\right)^{9/10}\right]^{-1/9} \quad \text{and} \tag{21a}$$

$$\mathrm{St}(\mathrm{Re}_{x_{99}}) = 0.0287\,\mathrm{Re}_{x_{99}}^{-1/5}\mathrm{Pr}^{-2/5}\frac{\ln(1+B_h)}{B_h}\left[1-\left(\frac{x_{99}-x_{T_{01}}}{x_{99}}\right)^{9/10}\right]^{-1/9} \quad \text{with} \quad B_h = \frac{F}{\mathrm{St}} \tag{21b}$$

as representative correlations for the heat transfer of a non transpiration cooled and a transpiration cooled test case in dependence of the axial Reynolds number $\mathrm{Re}_{x_{99}}$. Those are compared to measurement data in Fig. 9 (left). In this context the reference values St_0 of the uncooled case are not depicted, since a determination by experimental data is quite vague due to small temperature gradients and higher measurement uncertainties which lead to a determination of the Stanton number by a rather fluctuating straight line than a unequivocal temperature profile. However, a qualitatively good agreement for the first test case with transpiration cooling across all samples can be seen. After leaving starting length effects behind the calculated measurement values meet the correlations extremely well. Regarding the second test case the starting length effects seem to dominate across to whole length of the cooled probe never reaching the correlation values and consequently, once more, indicating that the representation with the axial Reynolds number $\mathrm{Re}_{x_{99}}$ seems not to be ideal. However, interesting to mention for test case 2 is the collapse of the Stanton numbers over the forth not perfused sample towards the unblown reference, showing similarities of the investigations by Whitten and Kays [38, 39] of a nonuniform blowing situation, which, however, were preferably formed with the enthalpy thickness Reynolds number Re_{δ_h}. Furthermore, limitations have to be set on higher blowing ratios of $F < 0.5$%, again, which can be explained focusing on the momentum reduction representation in Fig. 7 (right) and the heat reduction representation in Fig. 9 (right). Here, a comparison is made on the model of Kays [9], which goes back onto investigations of Mickley [40]. Consequently, dividing Eq. (21a) and (21b) and minor arrangements the heat reduction

$$\left.\frac{\mathrm{St}}{\mathrm{St}_0}\right|_{\mathrm{Re}_{x_{99}}} = \frac{b_h}{e^{b_h}-1} \quad \text{with the blowing parameter} \quad b_h = \frac{F}{\mathrm{St}_0} \tag{22}$$

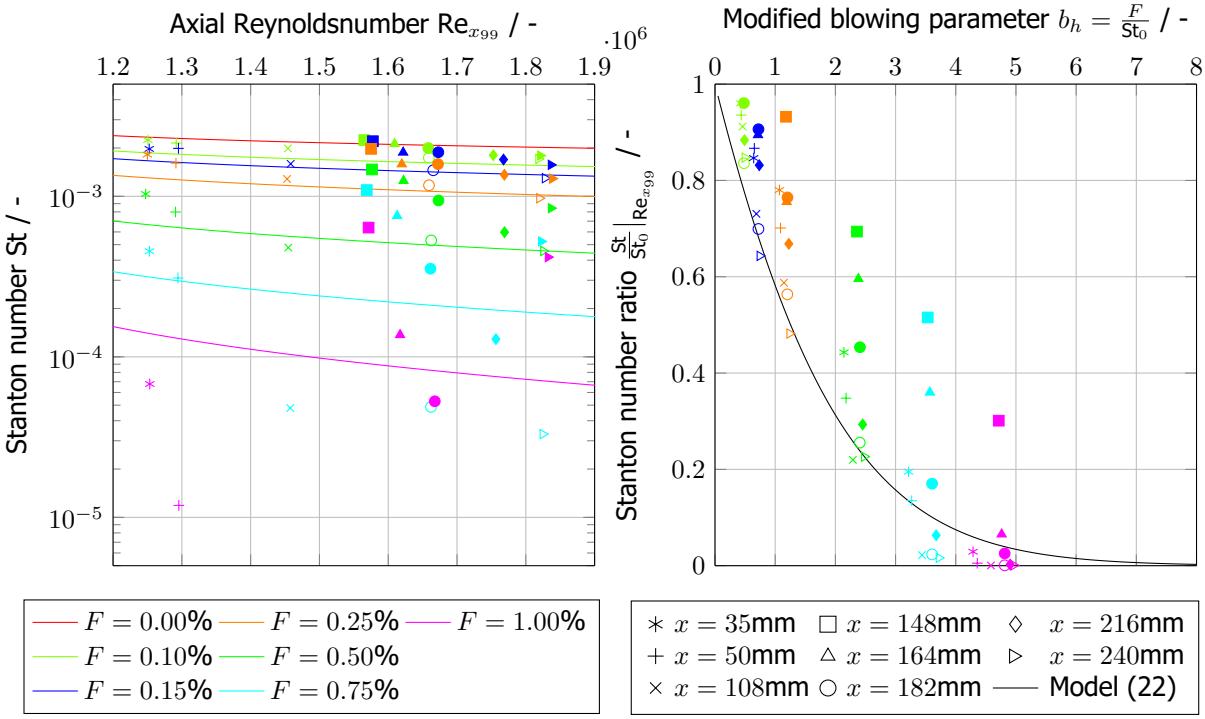

Figure 9. Representation of the Stanton number development along the axial running length in comparison with the respective correlations in Eq. (21a) and Eq. (21b) (left) and the exponential heat transfer reduction due to blowing at a specific location Re$_{x_{99}}$ (right); filled symbols indicate test case 2 (see Tab. 1)

can be described as an exponential decay in dependence of the blowing ratio F and the local Stanton number St$_0$ of the no blowing reference case calculated by the correlation in Eq. (21a). Again, starting length effects dominate the view of Fig. 9 (right) especially regarding test case 2. However, considering the boundary layer of a developed transpired boundary layer, the measured Stanton numbers meet the correlation in Eq. (22) more accurately. Nevertheless, a unifying illustration of both similar test cases 1 and 2 cannot be reached with this representation of an axial Reynolds number Re$_{x_{99}}$ as already seen in case of the momentum transfer in Sec. 6.
Regarding higher blowing ratios of $F < 0.5\%$ in both considerations of the momentum and heat transfer in Fig. 7 (right) and 9 (right) the ratios of cooled and uncooled reference case are turning zero. This might be explained by a thickening transpired coolant film reaching a point of detachment and separation of the wall. In literature this effect is often called blow off and usually limited in $F \approx 1\%$ or $b_f = 4$ as given in Kays et al. [9] for an isothermal test case or temperature dependent with $b_f \approx 4 - 9$ for cooler wall surfaces in Kutateladze and Leont'ev [41, 42]. This is in good agreement with the demonstrated data in Fig. 7 (right). One consequence of this is also the dwindling heat reduction due to the lifted boundary layer, which is finally also visible in the Stanton number reatio representation in Fig. 9 (right).

9. Stanton numbers in dependence of the enthalpy thickness Reynolds number Re$_{\delta_h}$

As already stated by Whitten [38] in 1970 the Stanton number can be expressed only by local descriptors, the enthalpy thickness Reynolds number Re$_{\delta_h}$ and the blowing ratio F even for non-uniform blowing situations. In this context the representation of measured Stanton numbers over calculated enthalpy thickness Reynolds numbers Re$_{\delta_h}$ is expected to successfully implement the effort to map both test cases to each other with regard to heat transfer consideration by a clever choice of the dominating dimensionless parameters. The respective enthalpy thickness Reynolds numbers Re$_{\delta_h}$ can be determined

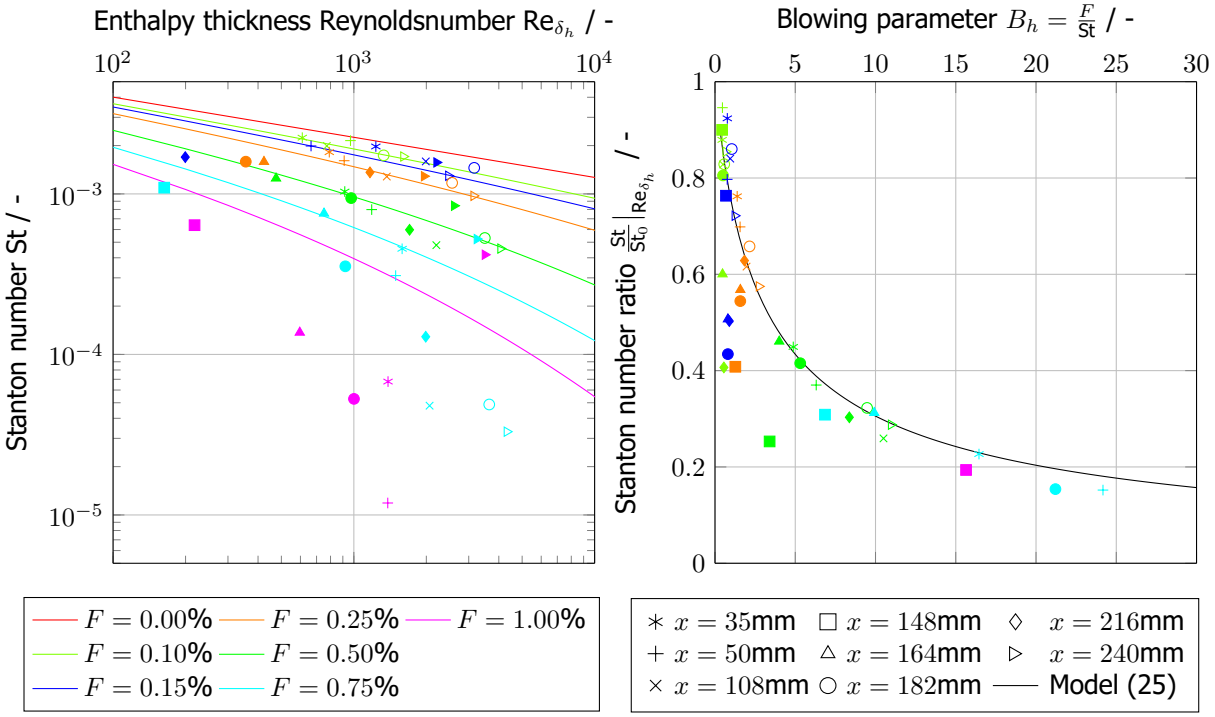

Figure 10. Illustration of the Stanton number in dependence of the enthalpy thickness Reynoldsnumber Re$_{\delta_h}$ with adapted correlations in Eq. (24a) and (24b) by a prefactor $C = 0.0106$ (left) and the exponential heat transfer reduction due to blowing at comparable enthalpy thickness Reynoldsnumber Re$_{\delta_h}$ (right); filled symbols indicate test case 2 (see Tab. 1)

by integration of the temperature profiles according to the compressible formulation of the enthalpy thickness

$$\delta_h = \int_0^{\delta_{T_{01}}} \frac{\rho u}{\rho_\infty u_\infty} \left(\frac{c_p T - c_{p_\infty} T_\infty}{c_{p_W} T_W - c_{p_\infty} T_\infty} \right) dy \tag{23}$$

with the local heat capacity c_p gained from the thermophysical gas property tables provided by NIST REFPROP data base [23]. Rearranging the previous formulations of the Stanton numbers in Eq. (21a) and (21b) with respect to the enthalpy thickness according to Kays [9], one can derive the expressions

$$\mathrm{St}_0\,(\mathrm{Re}_{\delta_h}) = 0.0125\ \mathrm{Re}_{\delta_h}^{-1/4}\mathrm{Pr}^{-1/2} \qquad \text{and} \tag{24a}$$

$$\mathrm{St}\,(\mathrm{Re}_{\delta_h}) = 0.0125\ \mathrm{Re}_{\delta_h}^{-1/4}\mathrm{Pr}^{-1/2} \left[\frac{\ln(1+B_h)}{B_h} \right]^{5/4} (1+B_h)^{1/4} \quad \text{with} \quad B_h = \frac{F}{\mathrm{St}}. \tag{24b}$$

Due to the similarity to Eq. (19a) and (19b) representing the friction coefficients and based on a comparable derivation, once again the prefactor adjustment from $C = 0.0125$ to $C = 0.0106$ was adopted to also further stay consistent within the representations in this paper. These adjusted correlations and the measured Stanton numbers are shown in Fig. 10 (left) whilst again no measured Stanton numbers St$_0$ of the no blowing reference are depicted due to the reasons mentioned previously. In comparison with the representation of the heat transfer by the axial Reynolds number Re$_{x_{99}}$ in Fig. 9, this time with the illustration of the heat transfer by the enthalpy thickness Reynolds number Re$_{\delta_h}$ shows a good agreement within the scope of measurement accuracy for both test cases. Even though starting length effects are still present and limitations regarding the applicability for blowing ratios of $F < 0.75\%$ have to be made the application of the the enthalpy thickness Reynolds number Re$_{\delta_h}$ looks promising. A final evaluation can be done by the representation of the heat reduction by blowing in Fig. 10 (right)

in comparison with the model

$$\left.\frac{\mathrm{St}}{\mathrm{St}_0}\right|_{\mathrm{Re}_{\delta_h}} = \left[\frac{(1+B_h)}{B_h}\right]^{5/4} (1+B_h)^{1/4} \quad \text{with} \quad B_h = \frac{F}{\mathrm{St}} \tag{25}$$

also stated in Kays [9] and gained by division of both Eq. (24a) and (24b). Herein, a general similarity and solid agreement with the described models is obvious, subsequently they can be used as an unifying description for the experimental test case. However, a deviation in the area of smaller blowing ratios F cannot be overseen. This might be explained by either the general intricacy in the determination of Stanton numbers, or unfavorable effects of the experimental setup as heat conduction in the metallic separation of the porous samples as well as a peculiarity of the test facility with a not totally perfect temperature entrance profile. This further makes it difficult to accurately determine a unique and precise boundary layer height $\delta_{T_{01}}$, which also leads to uncertainty in the calculation of the enthalpy thickness δ_h due to the dependency of $\delta_h = \delta_h\left(\delta_{T_{01}}\right)$.

10. Reynolds analogy: Relation between momentum and heat transfer

The ratio of momentum transfer and heat transfer in turbulent boundary layers is commonly known under the name Reynolds Analogy. In this context, in Meinert [26] an overview of numerous correlations for the uncooled reference case is summarized. Usually characterized by the Prandtl number Pr of the fluid a constant value for the ratio of $\mathrm{St}_0/\left(c_{f_0}/2\right)$ can be calculated which is in the order of magnitude of approx. $1.1-1.3$. In case of blowing, correlations are more rarely found, however, in Whitten [12] a representation for the Reynolds analogy with blowing can be found. Furthermore, Meinert [26] formulated

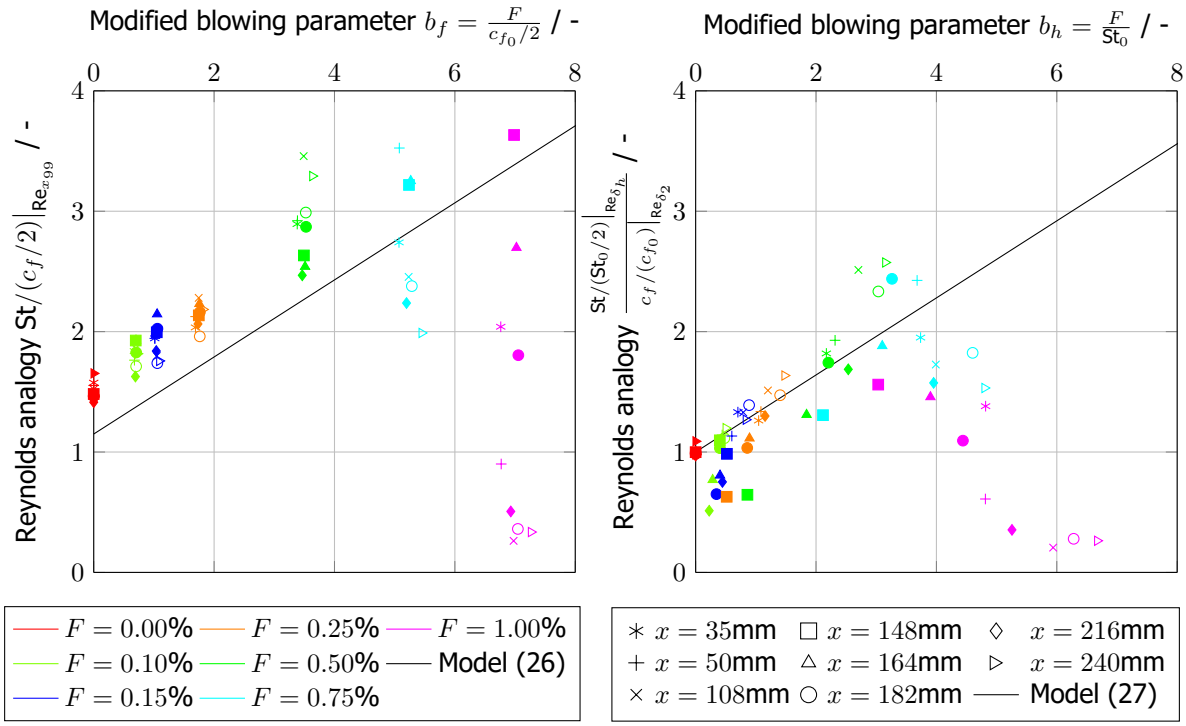

Figure 11. Visualization of the Reynolds Analogy $\mathrm{St}_0/\left(c_{f_0}/2\right)$ at various axial positions (left) in comparison with the Model of Meinert [26] and a modified illustration of the Reynolds analogy considering local uncooled references at an identical momentum thickness Reynolds number Re_{δ_2} and enthalpy thickness Reynolds number Re_{δ_h} (right); filled symbols indicate test case 2 (see Tab. 1)

a correlation for the Reynolds analogy by

$$\left.\frac{\mathrm{St}}{(c_f/2)}\right|_{\mathrm{Re}_{x_{99}}} = a_0 + a_1 \frac{F}{(c_{f_0}/2)} \quad \text{with} \quad a_0 = 1.15 \approx \frac{1}{\mathrm{Pr}^{2/5}} \quad \text{and} \quad a_1 = 0.32. \tag{26}$$

In this regard, the coefficients a_0 and a_1 are fitted on measurement data of Meinert, who also investigated foreign gas injection, which influence is neglected here formula-wise. In contrast to first assumptions of Meinert, the coefficient a_0 can also be calculated by deriving Eq. (17a) and (21a) consequently expressing $a_0 = a_0(\mathrm{Pr})$ as a function of the Prandtl number and representing the ratio of $\mathrm{St}_0/(c_{f_0}/2)$. The derived ratios are presented in Fig. 11 (left) in dependence of the modified blowing parameter b_f build with the measured values of the friction coefficient c_{f_0}. Here, the values for St_0 are again determined by the correlation in Eq. (21a). Similar to the previous sections, where a local axial propagation could be seen for the friction coefficients c_f and the Stanton numbers St, also in the ratio of both parameters an axial propagation can be identified. Nevertheless, the values line up on a straight line slightly shifted to the correlation by Meinert in Eq. (26). This shift can mostly be explained by the unheated starting length influence leading to increased Stanton numbers than with an identical starting length of the kinematic and thermal boundary layer. Furthermore, for higher blowing ratios of $F > 0.5\%$ first deviations of this straight line occur, until the values abruptly tend to zero and the previous mentioned blow off situation occurs.
An alternative representation with an independent formulation of the unheated starting length can be reached dividing Eq. (26) by $a_0 = \mathrm{St}_0/(c_{f_0}/2)$ turning to

$$\left.\frac{\frac{\mathrm{St}}{\mathrm{St}_0}\big|_{\mathrm{Re}_{\delta_h}}}{\frac{c_f}{c_{f_0}}\big|_{\mathrm{Re}_{\delta_2}}}\right|_{\mathrm{Re}_{x_{99}}} = 1 + a_1 b_h \quad \text{with} \quad b_h = \frac{F}{\mathrm{St}_0|_{\mathrm{Re}_{\delta_h}}}. \tag{27}$$

As proven to be advantageous in Sec. 7 and Sec. 8 the corresponding reference values for the uncooled test case are calculated by Eq. (19a) and (24a) with an adapted prefactor of $C = 0.0106$ at an identical momentum thickness Reynolds number Re_{δ_2} and an enthalpy thickness Reynolds number Re_{δ_h}. With a visualization in Fig. 11 (right) an solid agreement with the model is obvious until blow off can be identified with the ratios break down to zero. Even though the inaccuracies of the Stanton ratio representation in Fig. 10 continue here and are recognizable again, a general validity of the newly derived model can be notified, which illustrates the measured values for both test cases in an unifying representation again.

11. Summary

In a stacked transpiration cooling setup of porous carbon fiber reinforced carbon (C/C) samples two different test cases of variable injection lengths with diverging starting points are considered. Investigations in the hot gas channel at $T_{HG} \approx 374.15\,\mathrm{K}$ and $\mathrm{Re}_{Dh} \approx 200.000$ with a measurement rake traversable in x- and y-direction enable a survey of velocity and temperature profiles along the transpiration length to describe the influence of the injected coolant. Thereby, a wide range of blowing ratios up to $F = 4\%$ are investigated, wheres the characteristic of blow off is obvious already in the velocity and temperature profiles and could further be confirmed by a reduction of the friction coefficients tending to zero. Consequently, a limitation is made to the measurement data of blowing ratios of up to $F = 1\%$. Further focus is set on the channel specific boundary layer situation revealing an unheated starting length situation, respectively different starting lengths of kinematic and thermal boundary layer. In the following local friction coefficients and Stanton numbers in case of no blowing and blowing are determined for both test cases in order to characterize the local momentum transfer and heat transfer. Aiming an unifying illustration for both test cases different representations of both dimensionless values are compared. Whereas a description along the axial running length in form of the axial Reynolds number $\mathrm{Re}_{x_{99}}$ is quite common, for the skin friction coefficient a formulation with respect to the momentum thickness Reynolds number Re_{δ_2} as well as for the Stanton number a representation with respect to the enthalpy thickness Reynolds number Re_{δ_h} is advantageous and leads to an united description of both test cases. Concluding, the ratio of momentum and heat transfer, respectively the Reynolds Analogy, is investigated in more detail. In this regard a correlation of Meinert [26] is applied and juxtaposed an alternative formulation, which proved to be a valid approach, too.

Acknowledgments

Financial support has been provided by the German Research Foundation (Deutsche Forschungsgemeinschaft – DFG) in the framework of the Sonderforschungsbereich Transregio 40.

References

[1] Eckert, E. R. G. and Livingood, J. N. B. Comparison of Effectiveness of Convective Transpiration and Film Cooling Methods with air as coolant. *NACA Technical Note 3010*, 1953.

[2] S. Schweikert. *Ein Beitrag zur Beschreibung der Transpirationskühlung an keramischen Verbundwerkstoffen*. Ph.D. Thesis, University of Stuttgart, 2019.

[3] T. Langener. *A contribution to Transpiration Cooling for Aerospace Applications Using CMC Walls*. PhD thesis, University of Stuttgart, 2011.

[4] McKeon, B., Li, J., Jiang, W., and Morrison, J.and Smits, A. Pitot probe corrections in fully developed turbulent pipe flow. *Measurement Science and Technology*, 14, 08 2003.

[5] S. C. C. Bailey, M. Hultmark, J. P. Monty, P. H. Alfredsson, M. S. Chong, R. D. Duncan, J. H. M. Fransson, N. Hutchins, I. Marusic, B. J. McKeon, and et al. Obtaining accurate mean velocity measurements in high reynolds number turbulent boundary layers using pitot tubes. *Journal of Fluid Mechanics*, 715:642–670, 2013.

[6] F. H. Clauser. Turbulent Boundary Layers in Adverse Pressure Gradients. *Journal of the Aeronautical Sciences*, 21(2):91–108, 1954.

[7] T. N. Stevenson. A law of the wall for turbulent boundary layers with suction or injection. *College of Aeronautics Report*, 1963.

[8] P. Bradshaw. Comments on "Temperature Laws for a Turbulent Boundary Layer with Injection and Heat Transfer. *AIAA Journal*, 8(7):1375–1376, 1970.

[9] W. M. Kays, M. E. Crawford, and B. Weigand. *Convective Heat and Mass Transfer*. McGraw-Hill, 4th edition, 2005.

[10] Simpson, R. L. *The turbulent boundary layer on a porous plate: an experimental study of the fluid dynamics with injection and suction*. PhD thesis, Stanford University, 1967.

[11] Moffat, R. J. and Kays, W. M. The Turbulent Boundary Layer on a Porous Plate: Experimental Heat Transfer with Uniform Blowing and Suction. *International Journal of Heat and Mass Transfer*, 1968.

[12] Whitten, D. G., Kays, W. M., and Moffat, R. J. The turbulent boundary layer on a porous plate : experimental heat transfer with variable suction, blowing and surface temperature. *Stanford University, HTM-3, Forschungsbericht*, 1967.

[13] D. Prokein, J. von Wolfersdorf, C. Dittert, and H. Böhrk. Transpiration Cooling Experiments on a CMC Wall Segment in a Supersonic Hot Gas Channel. *AIAA Propulsion and Energy Forum, International Energy Conversion Engineering Conference, Cincinnati, Ohio*, 2018.

[14] W. Sutherland. *The viscosity of gases and molecular force*. Philosophical Magazine Series 5, S. 507-531, 1893.

[15] F. M. White. *Viscous fluid flow*. McGraw-Hill, 1991.

[16] B. Heidenreich. Manufacture and applications of C/C-SiC and C/SiC composites. *Ceramic Transactions*, 234, 09 2012.

[17] M. Selzer, S. Schweikert, H. Böhrk, H. Hald, and J. von Wolfersdorf. Comprehensive C/C sample characterizations for transpiration cooling applications. *Sonderforschungsbereich/Transregio 40 - Annual Report 2016, 61-72*, 2016.

[18] A. Trübsbach, A. Schwab, M. Selzer, H. Böhrk, and J. von Wolfersdorf. Integration of a test setup for transpiration cooling. *Sonderforschungsbereich/Transregio 40 - Annual Report 2018, 71-83*, 2018.

[19] Schmirler, M. and Krubner, J. Double probe recovery temperature Anemometry. *Thermal Science and Engineering Progress*, 23:100875, 2021.

[20] E. Eckert and O. Drewitz. *Der Wärmeübergang an eine mit großer Geschwindigkeit längs angeströmte Platte*. Forschung auf dem Gebiet des Ingenieurwesens A, 11th edition, 1940.

[21] E. R. G. Eckert and Jr. Drake, R. M. *Heat and mass transfer*. McGraw-Hill Book Company, 2nd edition, 1959.

[22] S. Chung. Survey of literature on convective heat transfer coefficients and recovery factors for high atmosphere thermometry. *NASA Technical Report*, 1973.

[23] E. W. Lemmon, I. H. Bell, M. L. Huber, and M. O. McLinden. NIST Standard Reference Database 23: Reference Fluid Thermodynamic and Transport Properties-Refprop, Version 10.0, National Institute of Standards and Technology, 2018.

[24] H. Blasius. *Grenzschichten in Flüssigkeiten mit kleiner Reibung*. PhD thesis, Universität Georgia Augusta zu Göttingen, 1907.

[25] D. Surek and S. Stempin. *Angewandte Strömungsmechanik*. Vieweg & Teubner, 2007.

[26] Meinert, J. *Haftreibung und Wärmeübergang in einer turbulentenGrenzschicht bei Fremdgastranspiration*. PhD thesis, TU Dresden, 2000.

[27] Schlichting, H. and Gersten, K. *Grenzschichttheorie*. Springer-Verlag Berlin Heidelberg, 10th edition, 2006.

[28] Gersten, K. and Herwig, H. *Strömungsmechanik, Grundlagen der Impuls-, Wärme- und Stoffübertragung aus asymptotischer Sicht*. Vieweg & Sohn Verlagsgesellschaft mbH, 3rd edition, 1992.

[29] Ghiaasiaan, S. M. *Convective Heat and Mass Transfer*. CRC Press, 1st edition, 2018.

[30] Kreith, F., editor. *The CRC handbook of thermal engineering*. CRC Press, 1st edition, 2000.

[31] H. Schlichting. *Grenzschicht-Theorie*. G. Braunsche Hofbuchdruckerei und Verlag GmbH, 5th edition, 1965.

[32] Cebeci, T. *Analysis of Turbuent Flows with Computer Programs*. Butterworth-Heinemann, 3rd edition, 2013.

[33] Prandtl, L. and Betz, A. Über den Reibungswiderstand strömender Luft. *Ergebnisse der Aerodynamischen Versuchsanstalt zu Göttingen. III. Lieferung*, 1927.

[34] Rohsenow, M., Hartnett, J. P., and Cho, Y. I. *Handbook of Heat Transfer*. McGraw-Hill, 3rd edition, 1998.

[35] Isaacson, L. K. and AlSaji, S. J. Temperature Laws.for aTurbulent Boundary Layer with Injection and Heat Transfer. *AIAA Journal*, 7(1):157–159, 1969.

[36] Simpson, R. L., Moffat, R. J., and Kays, W. M. The turbulent boundary layer on a porous plate: experimental skin friction with variable injection and suction. *International Journal of Heat and Mass Transfer*, 12:p. 771–789, 1969.

[37] Simpson, R. L. The effect of a discontinuity in wall blowing on the turbulent incompressible boundary layer. *International Journal of Heat and Mass Transfer*, 1971.

[38] Whitten, D. G., Moffat, R. J., and Kays, W. M. Heat transfer to a turbulent boundary layer with nonuniform blowing and surface temperature. *Proceedings of the Fourth International Heat Transfer Conference, Paris - Versailles*, 1970.

[39] Kays, W. M. Heat transfer to the transpired turbulent boundary layer. *International Journal of Heat and Mass Transfer*, 1972.

[40] Mickley, H. S., Ross, R. C., Squyers, A. L., and Stewart, W. E. Heat, mass and momentum transfer for flow over a flate plate with blowing or suction. *Naca Technical Note 3208*, 1954.

[41] Kutateladze, S. S. and Leont'ev, A. I. *Turbulent Boundary Layers in Compressible Gases*. Edward Arnold Ltd., 1964.

[42] Kutateladze, S. S. and Leont'ev, A. I. *Heat Transfer, Mass Transfer and Friction in Turbulent Boundary Layers*. Hemisphere Publishing Corporation, 1990.